NUMERICAL STUDY OF FLOW REORIENTATIONS IN TURBULENT CONVECTION WITH A FREE-SLIP UPPER BOUNDARY

Joauma Marichal and Miltiadis V. Papalexandris
Institute of Mechanics, Materials and Civil Engineering
Université catholique de Louvain
1348 Louvain-la-Neuve, Belgium
joauma.marichal@uclouvain.be; miltos@uclouvain.be

ABSTRACT

A typical feature of turbulent convection is the Large Scale Circulation (LSC), which can be described as the principal convective structure and is driven by plume formation at both boundaries. Inside cubical geometries, the LSC orients itself along one of the diagonal planes. However, the plane and direction of circulation are not fixed in time and reorientation events of one or both of them take place. In this paper, we study the dynamic properties of reorientations for a pseudo-Rayleigh–Bénard set up that involves a free surface on top instead of a rigid wall. The basic motivation for this study is to better understand the flow phenomena during the early stages of a Loss-of-Coolant Accident in spent fuel pools. More specifically, we report on large-eddy simulations of turbulent thermal convection in a cubical domain with a heated bottom wall, a cooled free-slip boundary and with water as the working fluid. The Rayleigh numbers considered in our study range from 2×10^7 up to 1×10^8. Since the thermo-physical properties of water vary considerably across the flow domain, the Oberbeck–Boussinesq approximation is not invoked. First, we briefly highlight the influence of the free-slip boundary on the flow structure. The paper continues with a discussion and analysis of the dynamics of the LSC. A study of the properties and frequency of reorientation events is presented herein. Comparisons between the properties of the LSC in the standard Rayleigh–Bénard convection and the configuration described above are also provided.

KEYWORDS
Free surface, Large-eddy simulation, Large Scale Circulation, Flow reorientations, Thermal convection

1. INTRODUCTION

In this paper, we report on simulations of turbulent thermal convection in water pools. The motivation for this study comes from the need to better understand thermal convection during the early stages of a Loss-of-Coolant Accident (LOCA) in spent nuclear fuel pools (SFP). Following the Fukushima disaster [1, 2], it has been acknowledged that a better understanding of the relevant physical phenomena is necessary in order to mitigate the risks and consequences of a LOCA [3, 4].

More specifically, we consider convection of water in a cubic domain that is heated from below and cooled at a free surface which is approximated by a free-slip boundary. The selected Rayleigh numbers are considerably lower than the expected ones during a LOCA, $Ra = \mathcal{O}(10^{14} - 10^{15})$. In fact, the resolution requirements for numerical simulations with realistic values in SFP currently far exceed available computational resources. Accordingly, this study aims at providing physical insight of turbulent convection with a free surface and not simulating an actual LOCA scenario. The Rayleigh numbers investigated are $Ra = 2 \times 10^7$ and $Ra = 1 \times 10^8$. In this range of Rayleigh numbers, the turbulence intensity is moderate and the flow is characterized by a system of upward and downward plumes that lead to the formation of the so-called

Large Scale Circulation (LSC). The LSC is the principal convective structure in this range of Ra. The properties and structure of the LSC have been the topic of a considerable number of studies in the past [5–12]. In cuboidal domains, the LSC aligns itself to one of the diagonal planes. However, this alignment is not stationary and reorientation events occur over time. More specifically, the LSC may rotate from one plane to the other; this reorientation event is referred to as a *rotation*. Also, the LSC may temporarily cease before reappearing at another diagonal plane; this event is referred to as a *cessation* [13]. Reorientation events occur in an apparently random manner [7, 14, 15].

Our study is based on wall-resolved Large Eddy Simulation (LES) and focuses on the dynamic behavior of the LSC and the impact of the free surface on it. According to the LES approach, the large turbulent structures (which carry most of the turbulent kinetic energy) are resolved by the computational mesh whereas the smaller ones are properly modeled, thereby leading to significant computational savings over direct numerical simulations (DNS). Also, it provides more accurate and detailed predictions of the turbulence properties than Unsteady Reynolds-Averaged Navier-Stokes (URANS). In this particular case, it is by virtue of the LES approach that we can run simulations over sufficiently long time periods so as to draw conclusions about the frequency of reorientation events. For comparison purposes, we have also performed LES of the corresponding classical Rayleigh–Bénard convection, i.e. with a rigid wall on top, the results of which are also presented herein.

2. GOVERNING EQUATIONS

Typically, numerical studies of thermal convection invoke the Oberbeck–Boussinesq approximation, according to which the density variations are only taken into account in the gravity acceleration term. However, due to the relatively large temperature gradients present in the cases examined herein, the flow properties can no longer be assumed to be independent of the temperature. For this reason, our study is based on the low-Mach number approximation [16, 17] of the compressible Navier–Stokes–Fourier equations. In the context of LES, the governing equations are spatially filtered. For a generic quantity ϕ, the filtered quantity is denoted by $\overline{\rho\phi}$. Also, for purposes of convenience we introduce the density-weighted filtering operation, or Favre-filtering. The Favre-filtered quantity of ϕ is given by $\widetilde{\phi} = \frac{\overline{\rho\phi}}{\overline{\rho}}$. The resulting system of equation reads as follows:

$$\frac{\partial \overline{\rho}}{\partial t} + \boldsymbol{\nabla}\cdot\left(\overline{\rho}\widetilde{\boldsymbol{u}}\right) = 0\,, \tag{1}$$

$$\frac{\partial\left(\overline{\rho}\widetilde{\boldsymbol{u}}\right)}{\partial t} + \boldsymbol{\nabla}\cdot\left(\overline{\rho}\widetilde{\boldsymbol{u}}\widetilde{\boldsymbol{u}}\right) = -\boldsymbol{\nabla}\overline{p} + \boldsymbol{\nabla}\cdot\left(2\mu\widetilde{\boldsymbol{S}}\right) - \boldsymbol{\nabla}\cdot\boldsymbol{\tau}^{\mathrm{r}} + \overline{\rho}\boldsymbol{g}\,, \tag{2}$$

$$\frac{\partial\overline{\rho}c_p\widetilde{T}}{\partial t} + \boldsymbol{\nabla}\cdot\left(\overline{\rho}c_p\widetilde{\boldsymbol{u}}\widetilde{T}\right) = \frac{\mathrm{d}p_0\left(t\right)}{\mathrm{d}t} + \boldsymbol{\nabla}\cdot\left(\kappa\boldsymbol{\nabla}\widetilde{T}\right) + \boldsymbol{\nabla}\cdot\boldsymbol{q}^{\mathrm{r}}\,, \tag{3}$$

where $\overline{\rho}$ and $\widetilde{\boldsymbol{u}} = (\widetilde{u}, \widetilde{v}, \widetilde{w})$ stand, respectively, for the filtered fluid density and Favre-filtered velocity vector. In equation (2), μ is the dynamic viscosity, $\widetilde{\boldsymbol{S}}$ is the deviatoric component of the filtered strain-rate tensor and $\overline{p}$ is the sum of the (filtered) dynamic and bulk-viscous pressures [18, 19]. The dynamic pressure is obtained as the second term of the asymptotic expansion of the fluid pressure at low-Mach number. Finally, in equation (3), c_p is the specific heat capacity, κ the thermal conductivity and $p_0(t)$ the first term of the expansion of the fluid pressure, referred to as the thermodynamic pressure. According to the low-Mach number approximation, the thermodynamic pressure is a function of time only. For the cases considered herein it is set equal to the ambient pressure.

An isobaric "equation of state", $\overline{\rho}(\widetilde{T})$, linking the density to the temperature field is used to close the above system of equations. The latter takes the form of a seventh-order polynomial fit. The two transport coefficients, κ and μ as well as the specific heat capacity c_p are also given by polynomial fits over the relevant temperature range. The tabulated data used originates from [20].

Upon filtering of the Navier–Stokes–Fourier equations, the unresolved terms in the momentum equation (2) are represented as an additional, subgrid-scale stress tensor $\boldsymbol{\tau}^{\mathrm{r}}$,

$$\boldsymbol{\tau}^{\mathrm{r}} - \frac{1}{3}\mathrm{Tr}(\boldsymbol{\tau}^{\mathrm{r}}) \;=\; -2\mu_{\mathrm{t}}\widetilde{\boldsymbol{S}}\,, \tag{4}$$

while the unresolved terms in the energy equation (3) are modeled as an additional subgrid-scale heat flux $\boldsymbol{q}^{\mathrm{r}}$,

$$\boldsymbol{q}^{\mathrm{r}} \;=\; \lambda_{\mathrm{t}}\boldsymbol{\nabla}\widetilde{T}\,. \tag{5}$$

In equation 4, the residual kinetic energy term, $\frac{1}{3}\mathrm{Tr}(\boldsymbol{\tau}^{\mathrm{r}})$, is incorporated in the pressure term $\overline{p}$ of equation (2), while the eddy viscosity μ_{t} is given by,

$$\mu_{\mathrm{t}} \;=\; C_s\, k^{1/2}\,\Delta\,. \tag{6}$$

The model constant, C_s is obtained through the dynamic one-equation eddy-viscosity procedure described in [21, 22]. A transport equation is solved to acquire the subgrid kinetic energy k, while Δ stands for the cell size. Finally, the eddy conductivity of equation 5 is computed via the Reynolds analogy and gives:

$$\lambda_{\mathrm{t}} \;=\; \mu_{\mathrm{t}} c_p / Pr_{\mathrm{t}}\,. \tag{7}$$

In our study, the turbulent Prandtl number Pr_{t} is taken constant and equal to 0.4 as recommended in [23].

With regard to the numerical algorithm, equations (1)–(3) are integrated using a Finite Volume Method (FVM) on a collocated grid system. Time integration is performed via a backward scheme that involves the current and the two previous time steps, while the spatial-discretization is performed via second-order central differences. Further, a PISO-type (Pressure-Implicit with Splitting of Operators) projection method is used for the numerical treatment of the pressure-velocity coupling. This procedure involves solving a Poisson equation for $\overline{p}$ derived from a combination of the divergence of the momentum equation and the continuity equation [12, 24]. One should note that the simulations are performed with the framework of OpenFOAM via user-defined functions.

3. NUMERICAL SETUP

The computational domain is a cube of height h with adiabatic side walls. The temperatures at the lower and upper boundaries are maintained at temperatures T_{h} and T_{c} respectively, with $T_{\mathrm{c}} < T_{\mathrm{h}}$. The case of interest involves a free-slip upper boundary and will henceforth be referred to as FS. On the other hand, the case of classical Rayleigh–Bénard convection will be simply referred to as RBC. In both cases, a kinematic no-slip condition is applied at the lower boundary located at $y = 0$. In FS, the kinematic free-slip condition at the upper boundary reads $\frac{\partial u}{\partial y} = \frac{\partial w}{\partial y} = 0$ at $y = h$, while a no-slip condition is prescribed at $y = h$ in RBC.

Turbulent convection is governed by three dimensionless parameters: the Rayleigh and Prandtl numbers as well as the aspect ratio. The aspect ratio is fixed to one while the Raleigh and Prandtl numbers are defined as,

$$Ra \;=\; \frac{g\,\beta_{\mathrm{ref}}\,h^3\,\Delta T}{\nu_{\mathrm{ref}}\,\kappa_{\mathrm{ref}}}\,, \quad \text{and} \quad Pr \;=\; \frac{\nu_{\mathrm{ref}}}{\alpha_{\mathrm{ref}}}\,, \tag{8}$$

respectively. As mentioned in the introduction, herein we consider two different cases, with Rayleigh numbers $Ra = 2\times10^7$ and $Ra = 1\times10^8$, respectively. The reference thermo-physical properties are found to be those of water at the reference temperature, T_{ref}. The latter is equal to the mean between the top and bottom temperatures, $T_{\mathrm{ref}} = (T_{\mathrm{h}} + T_{\mathrm{c}})/2$, while the reference temperature difference is defined as $\Delta T = T_{\mathrm{h}} - T_{\mathrm{c}}$. As part of this study, $T_{\mathrm{ref}} = 353.15$ K and the corresponding properties are given in Table I. At the reference temperature, the Prandtl number of the water is found to be $Pr = 2.23$.

Further, the domain's height h, free-fall velocity $u_{\mathrm{ff}} = \sqrt{\beta_{\mathrm{ref}}\, g\, h\, \Delta T}$ and free-fall time $t_{\mathrm{ff}} = h/u_{\mathrm{ff}}$ are used as reference quantities for non-dimensionalization proposes. The values of these reference quantities for the two different cases examined in this study are provided in Table II.

Table I. Reference temperature T_{ref}, temperature difference ΔT, thermal expansion coefficient β_{ref}, kinematic viscosity ν_{ref}, thermal conductivity κ_{ref} and thermal diffusivity α_{ref} of water. The corresponding Prandtl number is $Pr = 2.23$.

$T_{\mathrm{ref}}\ [K]$	$\Delta T\ [K]$	$\beta_{\mathrm{ref}}\ \left[\frac{1}{K}\right]$	$\nu_{\mathrm{ref}}\ \left[\frac{m^2}{s}\right]$	$\kappa_{\mathrm{ref}}\ \left[\frac{W}{m\,K}\right]$	$\alpha_{\mathrm{ref}}\ \left[\frac{m^2}{s}\right]$
353.15	10	6.36×10^{-4}	3.64×10^{-7}	6.67×10^{-1}	1.64×10^{-7}

Table II. Domain height h, free-fall velocity u_{ff}, and free-fall time u_{ff} for the two Rayleigh numbers considered herein.

Ra	$h\ [cm]$	$u_{\mathrm{ff}}\ \left[\frac{cm}{s}\right]$	$t_{\mathrm{ff}}\ [s]$
2×10^7	2.67	4.08	0.655
1×10^8	4.57	5.34	0.856

Table III. Grid properties. N is the number of cells. N_u and N_θ stand for the number of cells inside the hydrodynamic and thermal boundary layers, respectively; the values without parenthesis are the actual numbers of cells in the computational grid, while the values in parenthesis are the minimum requirements according to [25].

Ra	Type	N	N_u	N_θ
2×10^7	RBC	$50\times50\times50$	9 (4)	8 (3)
	FS	$46\times46\times46$	5 (5)	5 (4)
1×10^8	RBC	$74\times74\times74$	11 (5)	10 (4)
	FS	$70\times70\times70$	7 (6)	5 (5)

With regard to grid resolution, we follow the same approach as in [26, 27]. More specifically, close to the boundaries we apply the criterion put forward in [25] for wall-resolved numerical simulations. The criterion provides the minimum number of cells inside the hydrodynamic and thermal boundary layers. Also, for determining the grid resolution in the bulk of the computational domain, we employ two different scales, the Taylor micro-scale and a relaxed temperature micro-scale [26]. The largest computational cell should be smaller than both of these micro-scale. The mesh is then stretched from the smallest cells at the boundaries to the largest ones in the center via a hyperbolic-tangent expansion function. For more details on the resolution requirements and the grid generation approach, the reader is referred to [26, 27]. The grid properties are given in Table III for the different cases under study.

4. RESULTS

In this section we first discuss the impact of the free surface on the properties of the LSC via comparisons between the FS and RBC cases. Then, we focus on reorientation events. The characteristics and frequency of reorientations are defined and the influence of the boundary condition and Rayleigh number is discussed. Finally, we examine the effect of the LSC reorientation events on second-order turbulence statistics.

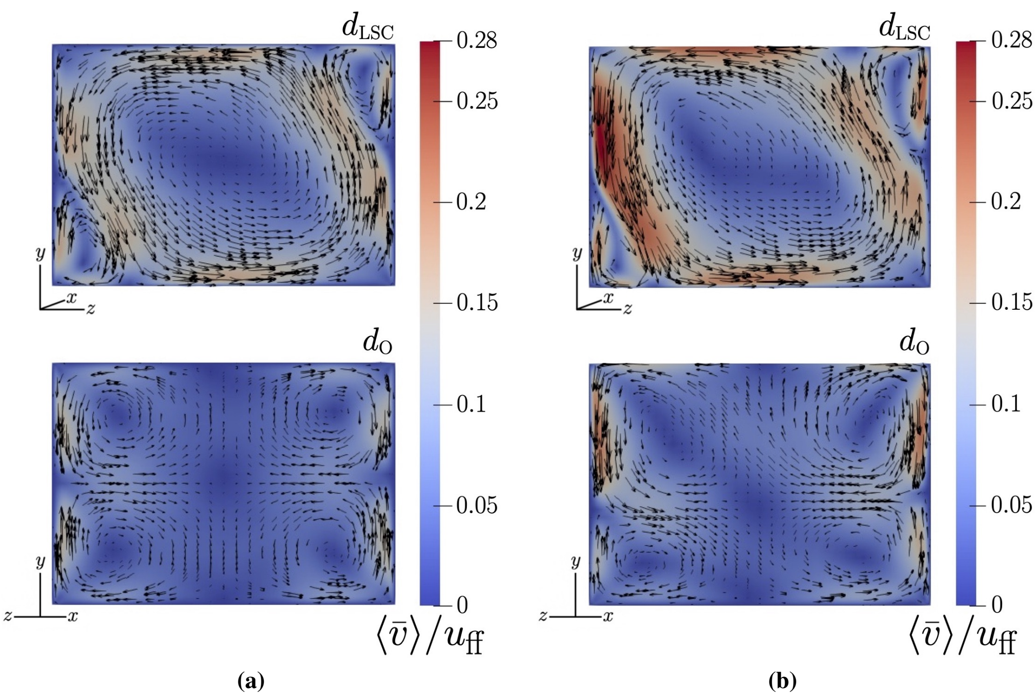

Figure 1. Color plots of the mean amplitude of the in-plane velocity component $\langle\bar{v}\rangle$, with superposed in-plane velocity vectors at the LSC plane d_{LSC}, and the orthogonal one d_{O}. The Rayleigh number is $Ra = 1 \times 10^8$. (a) RBC. (b) FS.

According to our simulations the predicted values of the global (time- and volume- averaged) Nusselt number for RBC are $Nu = 22.3$ at $Ra = 2 \times 10^7$, and $Nu = 36.6$ at $Ra = 1 \times 10^8$, which are very close to the correlation $Nu = 0.124Ra^{0.309}$ proposed in [15]. On the other hand, for FS the computed values of the global Nusselt number are markedly higher, namely $Nu = 29$ at $Ra = 2 \times 10^7$, and $Nu = 48$ at

$Ra = 1 \times 10^8$. These values are satisfactorily close to the correlation proposed by the authors of [24] for FS. The increase of Nu is attributed to the absence of hydrodynamic boundary layer at the top of the geometry, which favors convection [12, 26].

For the study of the main features and properties of the Large-Scale Circulation in RBC and FS we take averages of flow quantities over a period of 200 t_{ff} during which no reorientation events took place. This time period is deemed adequate for deducing the statistical properties of a stable LSC. In Figure 1, we provide plots of the time-averaged in-plane velocity components superposed with the corresponding in-plane velocity vectors for the two diagonal planes of the cubical domain. In these plots, we can observe that the upper counter-rotating vortices in the orthogonal diagonal plane are larger than the lower ones in FS while they have the same size in RBC. The same holds true for the corner rolls in the LSC plane. In other words, the free surface leads to a flow asymmetry. Also, since the free surface favors convection, in FS the downward motions of the fluid in the LSC and in the upper counter-rotating vortices are stronger than the corresponding upward ones.

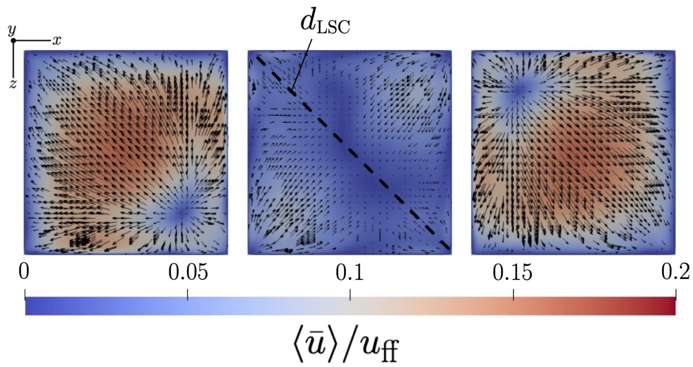

(a)

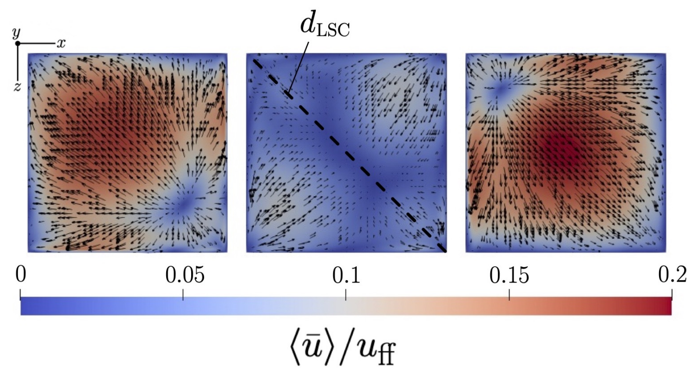

(b)

Figure 2. Color plot of the mean amplitude of the horizontal velocity component $\langle \bar{u} \rangle$, superposed with the corresponding vector plots, at horizontal planes for $Ra = 1 \times 10^8$. The horizontal planes are $y/h = 0.95$ (left), $y/h = 0.5$ (middle) and $y/h = 0.05$ (right). (a) RBC. (b) FS.

Plots of the amplitude of the time-averaged horizontal velocity superposed with the corresponding vectors, at three different horizontal planes, namely, $y/h = 0.95$, 0.50 and 0.05, are shown in Figure 2. We see that in RBC the plots at the planes $y/h = 0.95$ and $y/h = 0.05$ are mirror images of one another. This is no longer the case in FS. Moreover, it is clear that the amplitudes of the horizontal velocity component are higher in FS than in RBC. Once again, this is attributed to the free surface which reinforces convective motions by virtue of the absence of an upper hydrodynamic boundary layer. Interestingly though, the velocity amplitudes in FS are distinctively higher than in RBC even at the lower horizontal plane $y/h = 0.05$. In other words, the effect of the free surface on the emerging flow patterns is not limited to its vicinity but instead extends throughout the domain.

We next examine the frequency of reorientation events in both FS and RBC. The simulations are run for a long time period, $15\ 000\ t_{\rm ff}$, so as to register a sufficiently large number of reorientations in each case. As mentioned above, reorientation events can be either rotations or cessations. In cuboidal domains, there are two types of rotations. The first type consists of the change of alignment of the LSC from one diagonal plane to the other, whereas the second type consists of the inversion of the direction of the fluid motion within the LSC. Accordingly, the first type corresponds to a rotation of the LSC plane by an angle of $\pm\pi/2$ rads, whereas the second type corresponds to a rotation by an angle of π rads. On the other hand, cessations involve the temporary shutoff of the LSC and its reappearance at another diagonal plane.

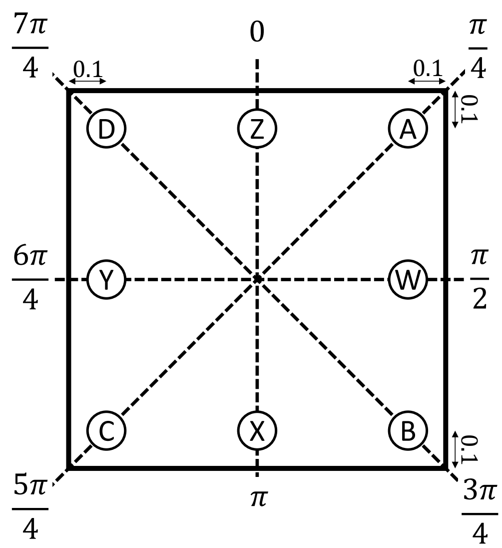

Figure 3. Horizontal plane located at $y/h = 0.5$ and showing the 8 probes used to record the vertical velocity.

For the purposes of our study we follow the methodology used by Foroozani et al [8] for the identification of reorientation events. In particular, we placed 8 probes in the horizontal mid-plane, located at azimuth angles of $\frac{i\pi}{4}$ with $i = 1...8$, and at a distance of $0.1h$ from their adjacent vertical wall, as shown in Figure 3. These probes record the vertical velocity as a function of time and allow us to define the orientation of the LSC.

As shown in Figure 1, the LSC is made of plumes rising near one corner and sinking at the opposite one. The vertical velocities recorded by the two probes located at the edges of the LSC plane are thus of similar magnitude but opposite sign. On the other hand, in the orthogonal plane, the counter-rotating vortices result in velocities of equal magnitude and zero mean at both sides of the plane. Figure 4 shows the time series of the vertical velocity at the four corner probes and allows the identification of the orientation of the LSC at all time.

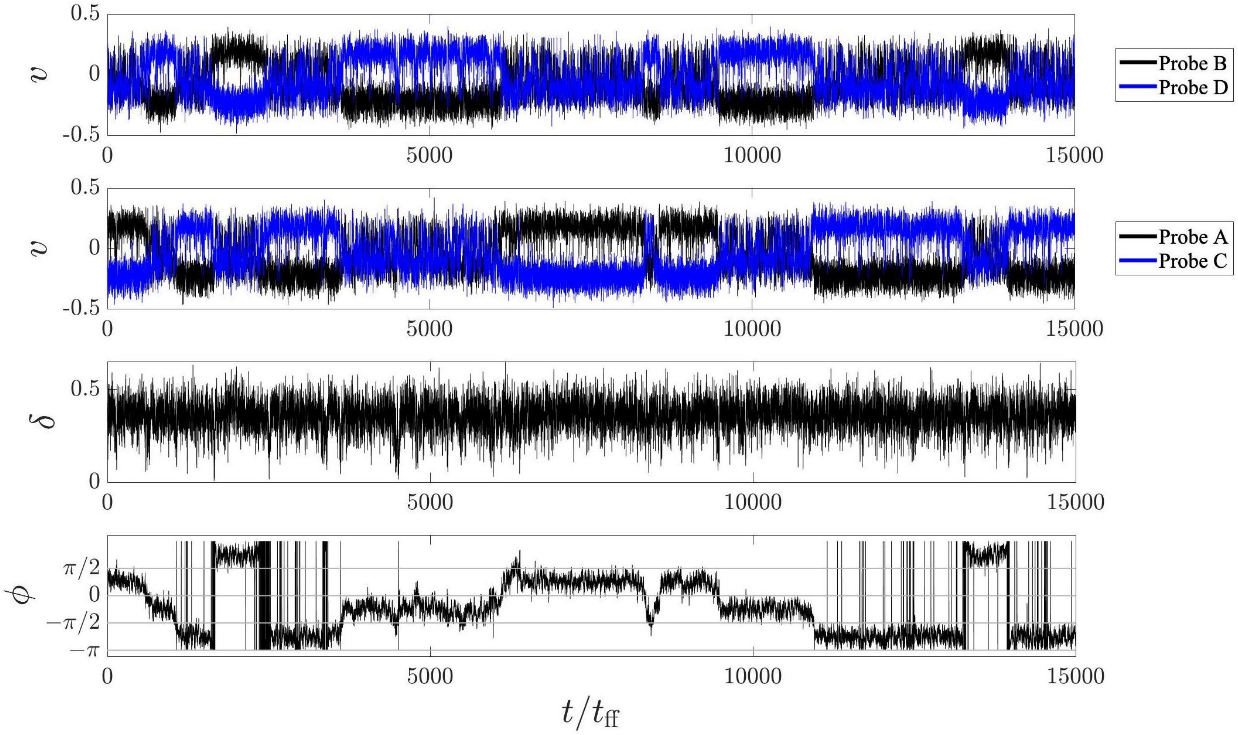

Figure 4. FS at $Ra = 1 \times 10^8$. Time series of the dimensionless vertical velocity v, amplitude δ and azimuth angle ϕ of the LSC, recorded by probes of the mid-height plane, $y/h = 0.5$. Initially, the LSC is oriented along the A-C diagonal, then at 650 t_{ff}, a reorientation takes place and the LSC moves to the B-D diagonal. Similar events continue to take place thereafter.

In order to improve reliably and better characterize reorientation events, 8 probes are employed for the calculation of the azimuth angle ϕ and amplitude δ of the LSC. The values of ϕ and δ are obtained via Fourier transform [8, 14],

$$\phi(t) \; = \; sgn\,(B_1(t)) \;\; \cos^{-1}\left(\frac{A_1(t)}{|\delta(t)|}\right), \qquad \delta(t) \; = \; \sqrt{A_1^2(t) + B_1^2(t)}\,. \tag{9}$$

with

$$A_1(t) \; = \; \frac{1}{2}\sum_{j=1}^{8} v_i(t)\cos(\theta_i)\,, \qquad B_1(t) \; = \; \frac{1}{2}\sum_{j=1}^{8} v_i(t)\sin(\theta_i)\,, \tag{10}$$

where v_i denotes the dimensionless velocity recorded at probe i and θ_i the azimuth angle of the same probe.

In Figure 4, we plot the values of ϕ and δ recorded by probes of the mid-height plane. Reorientations can be identified by changes of ϕ by $\pm\pi/2$ or π rads. Further, rotations can be distinguished from cessations on the basis of δ. More specifically, when a rotation takes place, no significant change of δ is observed. On the other hand, every time a cessation occurs, δ drops towards zero before recovering its average value.

According to the data provided by the probes, the most common type of reorientation is, by far, a rotation of the LSC by $\pm\pi/2$ rads, i.e. a change of plane of alignment. On the other hand, rotations by π rads are very rare. A few cases were observed for both RBC and FS at $Ra = 2 \times 10^7$ but none was recorded for the flows at $Ra = 1 \times 10^8$. Also, cessations have been observed in all four cases examined herein but are less frequent than rotations by $\pm\pi/2$ rads. These events are characterized by a drop of the amplitude δ towards zero and subsequent recovery towards its average value while the azimuth angle ϕ changes by $\pm\pi/2$ or π rads. This is in agreement with the findings reported in numerical studies [8,28]. To our knowledge, experimental data regarding reorientation frequency and characteristics are lacking.

Table IV. Total number of reorientation events, N_r over a time period of $15\,000\ t_\mathrm{ff}$ and corresponding reorientation frequencies f_r.

Ra	Type	N_r	f_r
2×10^7	RBC	37	0.0025
	FS	37	0.0025
1×10^8	RBC	14	0.0009
	FS	12	0.0008

In Table IV we provide the total number N_r, and frequency f_r, of reorientation events for all four cases considered in our study. The frequency of reorientation events is not affected by the choice of boundary condition. On the other hand, as the Rayleigh number increases, reorientation events become less frequent. This is in agreement with the findings reported in [28]. Also, in Figure 5 we plotted the cumulative number of reorientations as a function of time. Even though reorientations tend to occur spontaneously and in a random fashion, their frequency is constant in time. The plots in this figure corroborate further the fact that the free surface does not influence the reorientation frequency. Indeed, a single linear fit of the cumulative number of reorientations can be used for both RBC and FS.

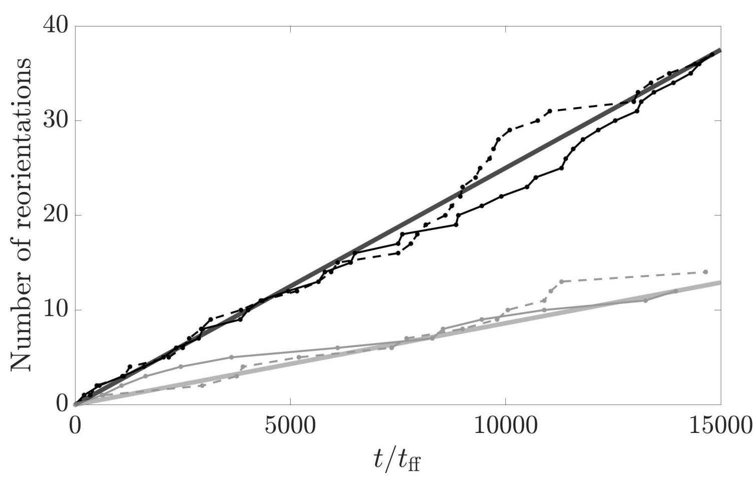

Figure 5. Cumulative number of reorientation events vs. time. Black lines are used for $Ra = 2\times10^7$: FS (——) and RBC (– –). Grey lines are used for $Ra = 1 \times 10^8$: FS (——) and RBC (– –). The dots signal the occurrence of a reorientation. Also, the thick solid lines are linear fits of the cumulative numbers of reorientations for FS at $Ra = 2 \times 10^7$ (▬) and $Ra = 1 \times 10^8$ (▬). The average duration of a specific flow orientation can be estimated from these data.

Another interesting aspect is the influence of reorientations on flow statistics. In order to fix ideas, let $\langle\ \rangle_{xz}$ denote time- and area-averaged quantities. The root-mean-square (rms) of the corresponding fluctuating components of the horizontal velocity, $\bar{u}_{\rm rms}$ is then defined as $\bar{u}_{\rm rms} = \sqrt{\langle u^2\rangle_{xz} - \langle u\rangle_{xz}^2 + \langle w^2\rangle_{xz} - \langle w\rangle_{xz}^2}$. Now let us consider the case of FS at $Ra = 1 \times 10^8$ and the reorientation event that takes place between $t \approx 580\ t_{\rm ff}$ and $630\ t_{\rm ff}$. Plots of $\bar{u}_{\rm rms}$ computed over different time-averaging periods, ranging from 450 to 950 $t_{\rm ff}$, are shown in Figure 6. Statistics taken over 450 and 550 $t_{\rm ff}$ do not include the aforementioned reorientation event, whereas statistics over longer periods do include it. From these plots, we see that before the reorientation, the $\bar{u}_{\rm rms}$ profiles are almost identical, i.e. the statistics are converged. However, after the reorientation, the profiles change considerably; more specifically, they increase and become flatter in the bulk. Further, it takes time before the profiles converge again.

A similar analysis has been performed for the rms of the normalized temperature, $\theta_{\rm rms} = \sqrt{\langle\theta^2\rangle_{xz} - \langle\theta\rangle_{xz}^2}$, and vertical velocity component, $v_{\rm rms} = \sqrt{\langle v^2\rangle_{xz} - \langle v\rangle_{xz}^2}$. However no changes in these rms profiles has been observed with increasing periods of time averaging so as to include the aforementioned reorientation event. One can therefore conclude that reorientation events have an effect on the rms of the horizontal velocity but not on the rms of the temperature and vertical velocity components.

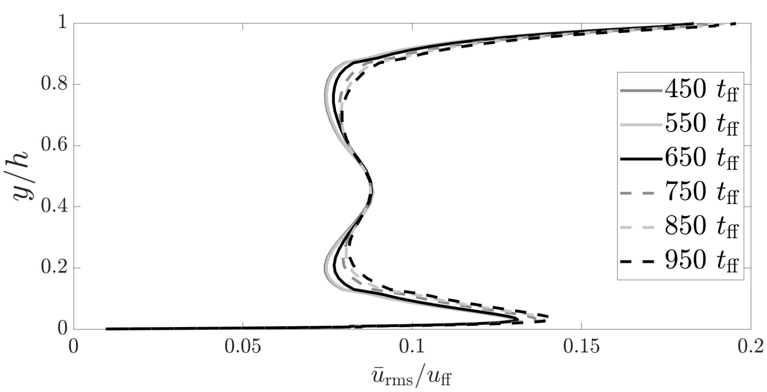

Figure 6. FS at $Ra = 1 \times 10^8$. Profiles of the rms of the horizontal velocity, $\bar{u}_{\rm rms}$, averaged over different time periods. A reorientation takes place from $t \approx 580\ t_{\rm ff}$ up to 630 $t_{\rm ff}$.

5. CONCLUSIONS

The effect of the free surface on turbulent convection in water pools heated from below has been studied via Large-Eddy Simulations. More specifically, we examined the structure and reorientation events of the Large-Scale Circulation (LSC), which is the principal convective structure in the flow of interest. Simulations of classical Rayleigh–Bénard convection have also been performed for comparison purposes. Our study confirmed that the presence of the free surface introduces a flow asymmetry and promotes convective motion. This leads to stronger downward motions of the fluid and an increase of the Nusselt number. Further, our study predicted that reorientation events occur spontaneously and in an apparently random fashion. Nonetheless the frequency of these events remains constant over time. Furthermore, according to our simulations, the frequency of reorientation events appears to be independent of the boundary condition on top. However the reorientation frequency is quite sensitive to the Rayleigh number; in particular it decreases considerably as the Rayleigh number is increased. Finally, our simulations showed that reorientation events have an impact on the second-order statistics of the horizontal velocity but not on those of the temperature and vertical velocity.

ACKNOWLEDGMENTS

The authors would like to thank Dr. William Hay for many fruitful discussions and suggestions. Further, they gratefully acknowledge the financial support provided by the Belgian Federal Ministry of Energy under the Energy Transition Fund, project SFP-LOCA. This work benefited from the computational resources provided by the supercomputing facilities of the Université catholique de Louvain (CISM/UCL) and the Consortium for high-performance computing and data storage of the Federation Wallonie Bruxelles (FWB), funded by the Belgian Fund of Scientific Research (F.R.S.- FNRS) under Convention No. 2.5020.11.

REFERENCES

1. National Academies of Sciences, Engineering, and Medicine, *Lessons Learned from the Fukushima Nuclear Accident for Improving Safety and Security of U.S. Nuclear Plants: Phase 2*, The National Academies Press, Washington, DC (2016)

2. N. Kan, *The Fukushima Nuclear Power Plant Disaster and the Future of Renewable Energy*, Cornell University Press (2018)

3. International Atomic Energy Agency, "IAEA Action plan on nuclear safety," (2011)

4. OECD (Nuclear Energy Agency), "Phenomena Identification and Ranking Table, R&D Priorities for Loss-of-Cooling and Loss-of-Coolant Accidents in Spent Nuclear Fuel Pools," (2018)

5. S. Cioni, S. Ciliberto, and J. Sommeria, "Experimental study of high-Rayleigh-number convection in mercury and water," *Dynam. Atmos. Oceans*, **24** (1), pp. 117–127 (1996)

6. K. Sugiyama et al., "Flow reversals in thermally driven turbulence," *Phys. Rev. Lett.*, **105**, pp. 034503 (2010)

7. P. Mishra, A. De, M. Verma, and V. Eswaran, "Dynamics of reorientations and reversals of large-scale flow in Rayleigh–Bénard convection," *J. Fluid Mech.*, **668**, pp. 480–499 (2011)

8. N. Foroozani, J. Niemela, V. Armenio, and K. Sreenivasan, "Reorientations of the large-scale flow in turbulent convection in a cube," *Phys. Rev. E*, **95**, pp. 033107 (2017)

9. N. Foroozani, J. Niemela, V. Armenio, and K. Sreenivasan, "Large eddy simulation of turbulent Rayleigh–Bénard convection in a cubic cell," *Proc. ERCOFTAC Ser., Vol. 24*, pp. 559–565, (2018)

10. D. Giannakis, A. Kolchinskaya, D. Krasnov, and J. Schumacher, "Koopman analysis of the long-term evolution in a turbulent convection cell," *J. Fluid Mech.*, **847**, pp. 735–767 (2018)

11. A. Castillo-Castellanos, A. Sergent, B. Podvin, and M. Rossi, "Cessation and reversals of large-scale structures in square Rayleigh–Bénard cells," *J. Fluid Mech.*, **877**, pp. 922–954 (2019)

12. W. A. Hay and M. V. Papalexandris, "Numerical simulations of turbulent thermal convection with a free-slip upper boundary," *Proc. R. Soc. A*, **475**, pp. 20190601 (2019)

13. E. Brown and G. Ahlers, "Rotations and cessations of the large-scale circulation in turbulent Rayleigh–Bénard convection," *J. Fluid Mech.*, **568**, pp. 351–386 (2006)

14. S. Cioni, S. Ciliberto, and J. Sommeria, "Strongly turbulent Rayleigh–Bénard convection in mercury: comparison with results at moderate Prandtl number," *J. Fluid Mech.*, **335**, pp. 111–140 (1997)

15. J. Niemela, L. Skrbek, K. Sreenivasan, and R. Donnelly, "Turbulent convection at very high Rayleigh numbers," *Nature*, **404**, pp. 837–40 (2000)

16. S. Paolucci, "Filtering of sound from the Navier–Stokes equations," *NASA STI/Recon Technical Report N*, **83**, pp. 26036 (1982)

17. B. Lessani and M. V. Papalexandris, "Time accurate calculation of variable density flows with strong temperature gradients and combustion," *J. Comput. Phys.*, **212**, pp. 218–246 (2006)

18. M. Georgiou and M. V. Papalexandris, "Direct numerical simulation of turbulent heat transfer in a T-junction," *J. Fluid Mech.*, **845**, pp. 581–614 (2018)

19. M. V. Papalexandris, "On the applicability of Stokes' hypothesis to low-Mach-number flows," *Continuum Mech. Therm.*, **32**, pp. 1245–1249 (2020)

20. E. W. Lemmon, M. L. Huber, and M. O. McLinden, *NIST Standard Reference Database 23: Reference Fluid Thermodynamic and Transport Properties - REFPROP*, 9.0 edition, 2010

21. A. Yoshizawa, "Statistical theory for compressible turbulent shear flows, with the application to subgrid modeling," *Phys. Fluids*, **29** (7), pp. 2152–2164 (1986)

22. W. W. Kim and S. Menon, "A new dynamic one-equation subgrid-scale model for large eddy simulations," *Proc. 33rd Aerospace Sciences Meeting and Exhibit, AIAA 95-0356*, (1995)

23. T. M. Eidson, "Numerical simulation of the turbulent Rayleigh–Bénard problem using subgrid modelling," *J. Fluid Mech.*, **158**, pp. 245–268 (1985)

24. W. A. Hay and M. V. Papalexandris, "Evaporation-driven turbulent convection in water pools," *J. Fluid Mech.*, **904**, pp. A14 (2020)

25. O. Shishkina, R. Stevens, S. Grossmann, and D. Lohse, "Boundary layer structure in turbulent thermal convection and its consequences for the required numerical resolution," *New J. Phys.*, **12**, pp. 075022 (2010)

26. W. A. Hay, J. Martin, B. Migot, and M. V. Papalexandris, "Turbulent thermal convection driven by free-surface evaporation in cuboidal domains of different aspect ratios," *Phys. Fluids*, **33**, pp. 015104 (2021)

27. J. Marichal and M. Papalexandris, "On the dynamics of the large scale circulation in turbulent convection with a free-slip upper boundary," (2021), *under review*

28. V. T. Vishnu, A. K. De, and P. K. Mishra, "Dynamics of large-scale circulation and energy transfer mechanism in turbulent Rayleigh–Bénard convection in a cubic cell," *Phys. Fluids*, **32** (9), pp. 095115 (2020)